PERGAMON

International Journal of Heat and Mass Transfer 45 (2002) 3089–3099

International Journal of HEAT and MASS TRANSFER

www.elsevier.com/locate/ijhmt

A Reynolds analogy for real component surface roughness

B.J. Belnap, J.A. van Rij, P.M. Ligrani *

Convective Heat Transfer Laboratory, Department of Mechanical Engineering, 50 S. Central Campus Drive, MEB 2202, University of Utah, Salt Lake City, Utah 84112, USA

Received 22 August 2001; received in revised form 8 January 2002

Abstract

A new Reynolds analogy equation is presented, which is based on flow and thermal behavior in a rectangular cross-section channel with real component surface roughness. This roughness is similar to that which exists on some turbine surfaces under extreme operating conditions, or on surfaces of other industrial devices, with deposit accumulation such as heat exchangers. Skin friction coefficient, Nusselt number, Stanton number, and performance factor experimental results are given over a range of Reynolds numbers for one polished smooth surface, and for two other surfaces with different levels of irregularly shaped and irregularly distributed, three-dimensional surface roughness. The Reynolds analogy deduced from these data, with such roughness, is important because it is different from Reynolds analogy equations for surfaces with uniformly shaped elements arranged in a regular, periodic pattern.

1. Introduction

The Reynolds analogy provides a relation between local surface Stanton numbers and local surface skin friction coefficients. Generally applied to gases, where the turbulent and molecular Prandtl numbers are approximately equal to 1.0, the Reynolds analogy is based on the equivalence of the turbulent eddy diffusivities for heat and momentum. For turbulent flows over smooth surfaces, the analogy is then given by

$$St = C_f/2. \tag{1}$$

However, even with equivalent eddy diffusivities, the analogy does not apply to all physical mechanisms responsible for heat and momentum transfer. This is because diffusion of heat in turbulent fluid at the *smallest scales* is always due to molecular conduction, whereas diffusion of momentum is due to chaotic motions and impacts between fluid eddies over a spectrum of sizes. According to Kays and Crawford [1], these differences exist because there is no mechanism for heat transfer which is analogous to the pressure mechanism for momentum transfer.

Accurate Reynolds analogy equations for flows over *rough surfaces* are important for the design and analysis of many different devices, including micro-scale and macro-scale heat exchangers, internal cooling passages of turbine airfoils, external surfaces of turbine airfoils, macro-scale and micro-scale passages for electronics cooling, atmospheric re-entry vehicles, and a number of bio-medical devices. For example, the Reynolds analogy is especially helpful for design and analysis of components in gas turbine engines. In one notable investigation [2], it is used to determine surface skin friction coefficients, drag forces, and aerodynamic efficiencies from airfoil surface heat transfer data. Accurate Reynolds analogies, when tied to surface roughness characteristics, can also lead to improved component life predictions, as well as to reduced design uncertainties, and lower production and part costs.

The different mechanisms for thermal and momentum transport are especially important in regard to relationships between Stanton numbers and skin friction coefficients which are applied to flows over rough surfaces. This is because of finite temperature drops due to heat transfer by conduction in the semi-stagnate fluid which exists around and between roughness elements, as

* Corresponding author. Tel.: +1-801-581-4240; fax: +1-801-585-9826.

E-mail address: ligrani@mech.utah.edu (P.M. Ligrani).

0017-9310/02/$ - see front matter
PII: S0017-9310(02)00042-X

Nomenclature

b	channel test section height
$C_f/2$	skin friction coefficient, $\tau/\rho V^2$
C_p	specific heat at constant pressure
D_h	hydraulic diameter
h	heat transfer coefficient, $q/(t_w - t_m)$
k	thermal conductivity
k	average roughness height
k_s	equivalent sandgrain roughness size
Nu	Nusselt number, $hD_h/k = StPrRe_{D_h}$
ΔP	static pressure change
Pr	Prandtl number, $\rho\nu C_p/k$
Pr_t	turbulent Prandtl number
q	local heat flux
Re_{D_h}	hydraulic diameter Reynolds number, VD_h/ν
Re_{k_s}	roughness Reynolds number, $Vk_s(C_f/2)^{1/2}/\nu$
S	rough surface flat reference area
S_f	total roughness frontal area
S_s	total roughness windward wetted surface area
St	Stanton number, $h/\rho VC_p$
St_k	conduction sublayer Stanton number for flows over rough surfaces
t_m	local mixed-mean temperature
t_w	local wall temperature
Δx	incremental streamwise distance
V	spatially-averaged velocity
w	channel test section spanwise width
x	streamwise coordinate measured from the entrance of the test section
z	spanwise coordinate measured from the spanwise centerline of the test section

Greek symbols

ρ	static density
ν	kinematic viscosity
τ	surface shear stress
Λ_s	modified Sigal and Danberg roughness parameter [8]

Subscripts

o	smooth wall value
s	smooth wall value
r	rough wall value

well as within roughness cavities at the surface [3]. To account for these effects in wall bounded flows which are fully rough, Dipprey and Sabersky [3] suggest an equation of the form

$$St = C_f/2/\left[1 + (C_f/2)^{1/2}\left(5.19Re_{k_s}^{0.2}Pr^{0.44} - 8.48\right)\right]. \quad (2)$$

This empirical equation is based on experiments conducted using granular close-packed roughness on the surfaces of pipes, and upon a "cavity vortex hypothesis" to account for flow behavior very near roughness elements [3]. Even though Eq. (2) is based on experiments conducted with internal flows, it is also used as a rough surface Reynolds analogy equation for boundary layer flows over external surfaces [2]. Kays and Crawford [1] present a simplified form of Eq. (2), also for fully rough flows, which is given by

$$St = \frac{C_f/2}{Pr_t + (C_f/2)^{0.5}(1/St_k)}. \quad (3)$$

Here, St_k is a conduction sublayer Stanton number, which accounts for the temperature drop in the conducting fluid near roughness elements. According to Dipprey and Sabersky [3], St_k is represented by an equation which is given by

$$St_k = CRe_{k_s}^{-0.2}Pr^{-0.44}, \quad (4)$$

where C is an empirical constant, equal to 5.19 for granular close-packed roughness, 6.37 for some types of two-dimensional roughness, and 0.80 for uniform spheres roughness.

Reynolds analogy equations, such as those given by Eq. (1), are also useful for comparisons with Nusselt numbers and skin friction coefficients in flows where these non-dimensional parameters are augmented relative to smooth wall values. In internal passages, the objective is often to produce augmented values of Nu/Nu_o, in conjunction with diminished values of $(C_f/2)/(C_f/2_o)$ [4,5]. Overall performance of such passages is then characterized by performance parameters such as $(Nu/Nu_o)/(C_f/2/C_f/2_o)^{1/3}$ [6]. The Reynolds analogy equation (1) then provides a reference line for comparison, and sometimes, an approximate upper limit on the most favorable behavior for such internal passages.

In the present study, a new Reynolds analogy equation is developed for similar roughness that exists on the external surfaces of gas turbine airfoils under extreme operating conditions, or on surfaces of other operating industrial devices, such as heat exchangers, with deposit accumulation. The surfaces are created using the same manufacturing methods and similar aging methods as are encountered on the surfaces of operating turbine airfoils. The equation, and the experimental results which are presented and employed to deduce this equation are then representative of the roughness which exists naturally for real operating component surfaces, rather than for the artificial roughness like that employed by other investigators [3]. Presented are local skin friction coef-

ficients, local Nusselt numbers, and local Stanton numbers for surfaces with three different levels of roughness:

(i) smooth (for baseline comparisons, denoted *smooth*),

(ii) irregular rough elements (denoted *rough1*),

(iii) irregular rough elements (denoted *rough2*).

Performance parameters, and magnitudes of $St/(C_f/2)$ are then determined from these measured quantities. All of these results are obtained in an internal channel with an aspect ratio of 8, arranged with the instrumented test plates installed on the two widest surfaces.

2. Rough test surfaces

Three-dimensional profilometry scans show that the roughness employed for the present study is a replica of the roughness present on operating device surfaces in practical applications, including the roughness due to aging, deposit accumulation, and oxidation. Fig. 1 shows an enlarged image of a portion of the *rough1* test surface, obtained from three-dimensional optical profilometry data. Notice that the highest peaks reach to about 200 μm on the vertical scale. The irregularity, non-uniformity, and three-dimensional nature of the roughness elements, including their irregular arrangement, are evident from this plot. The elements on the *rough2* surface are qualitatively similar to the ones shown in Fig. 1, except that they give a larger value of equivalent sandgrain roughness. This is discussed further in Section 4.1.

3. Experimental apparatus and procedures

3.1. Flow facility and test section

Fig. 2 shows a schematic diagram of the flow facility employed for the investigation. The facility is open-circuit, subsonic, and constructed of polycarbonate material. The inlet section consists of a rectangular bell mouth, followed by a honeycomb and two screens. From the inlet section, the airflow enters a 40 contraction ratio nozzle, and then a straight duct, which is 863.6 mm long with the same cross-section as the test section (50.8 mm by 6.35 mm). Because this inlet duct is 76.5 hydraulic diameters in length, the flow is fully developed at the entrance of the test section, which follows. After the airflow exits the test section, it enters a square plenum. This plenum opens into a circular tube with an ASME standard orifice plate at the center of its length. The flow then exits into another square plenum. Attached to the opposite side of this plenum is a 7.5 horsepower New York Blower size 1808 suction blower that pulls the air through the wind tunnel. Two valves in the walls of the second plenum are employed to adjust the mass flow through the facility. Some details of the test section are shown in Fig. 3. The coordinate system is also included in this figure. The different test surfaces employed are installed along the top and bottom walls of the test section. The sidewalls are then made of smooth polycarbonate material. Pressure taps are located on the sidewalls with streamwise spacing between adjacent taps of 2.54 cm through the test section.

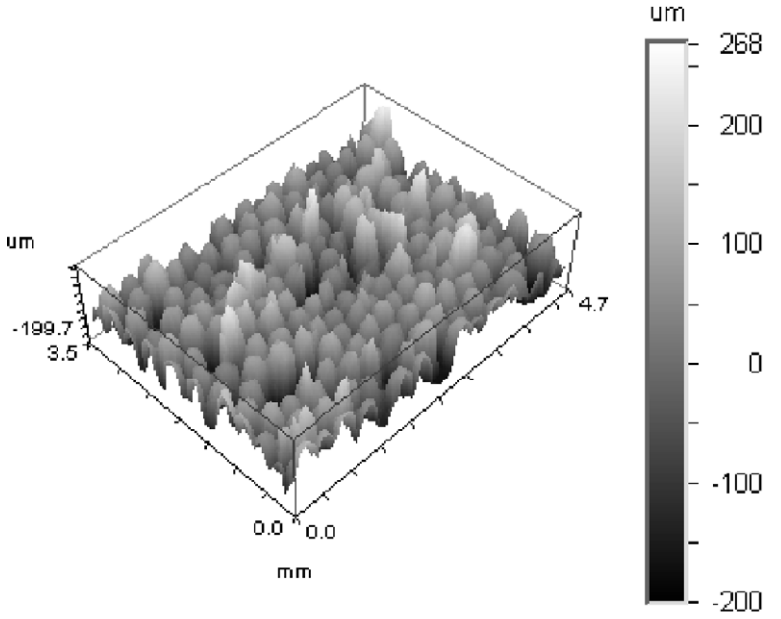

Fig. 1. Three-dimensional optical surface profilometry trace of a portion of the *rough1* test surface.

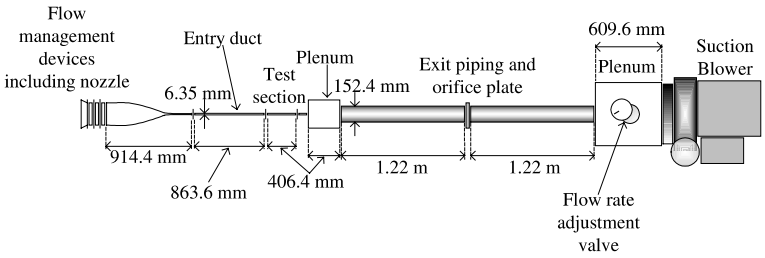

Fig. 2. Components and dimensions of the flow facility.

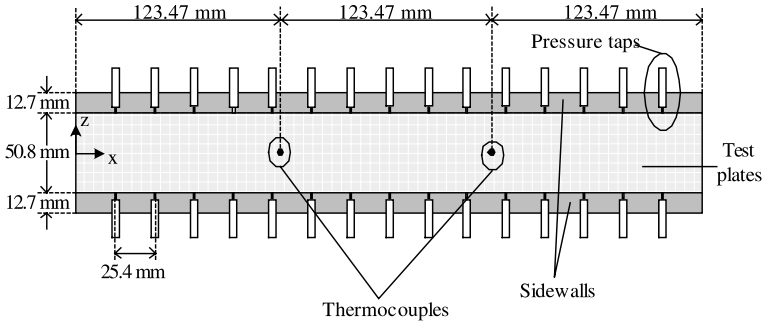

Fig. 3. Top view of the test section with the coordinate system employed.

The mass flow rate, spatially averaged velocity, and Reynolds number through the test section are determined using the measured pressure drop across the ASME standard orifice plate, and standard ASME procedures. To read the pressure drop, a Validyne 3-36 Model DP15-46, 1546N1S4A, S/N103378 pressure transducer with a D269-94A diaphragm is used. Signals from this device are processed using a Celesco CD10D Carrier-Demodulator. Voltages from the Carrier-Demodulator are acquired using a Hewlett-Packard type 44422A data acquisition card installed in a Hewlett-Packard HP3497A data acquisition controller and a HP 3498A extender. A Hewlett-Packard 362 series A4190A type computer system controls the data acquisition system, and is used to process experimental data. The pressure transducer is calibrated before each run using a Meriam manometer, model 40GD10-WM. During testing, 100 sequential pressure readings are acquired over a period of 1 min. With these procedures, Reynolds numbers based on hydraulic diameters of 10,000, 15,000, 20,000, 25,000, and 30,000 are employed. Note that the hydraulic diameter is determined from smooth surface channel dimensions.

3.2. Skin friction coefficient determination

Using conservation of momentum, the surface shear stress for all four channel surfaces is given by the equation having the form

$$\tau = (\Delta P/\Delta x)[bw/2(b+w)]. \tag{5}$$

The skin friction coefficient for the test section is then given by

$$C_f/2 = D_h(\Delta P/\Delta x)/4\rho V^2 \tag{6}$$

or alternatively,

$$C_f/2 = \tau/\rho V^2. \tag{7}$$

With this approach, $C_f/2$ values are representative of the top and bottom test surfaces (which can be either smooth or rough), as well as the two smooth sidewalls of the test section. Procedures to determine $C_f/2$ for the top and bottom test plates *only* are described later in this paper.

To measure $\Delta P/\Delta x$, pressures at five locations along the test section are made with respect to the most upstream pressure tap, which is located 25.4 mm from the beginning of the test section. The five locations where the pressure drop is measured are positioned 50.8, 76.2, 101.6, 152.4, and 177.8 mm from the upstream edge of the test section. Each pressure tap is connected to a Celesco LCVR pressure transducer. All transducers are calibrated prior to testing using the same Meriam model 40GD10-WM inclined manometer as a pressure standard. Signals from the transducers are processed using Celesco CD10D Carrier-Demodulators, and the other data acquisition equipment and computer described earlier.

3.3. Nusselt number and Stanton number determination

Custom-made Electrofilm etched-foil heaters, encapsulated between two thin layers of Kapton, are located on the outer surfaces of the top and bottom stainless steel test plates to provide a constant heat flux boundary condition. The entire test section is enclosed in three layers of 25.4 mm thick black neoprene foam insulation (with thermal conductivity of 0.035 W/mK) to minimize heat conduction losses. To measure the magnitudes of conduction heat losses, a total of 16 Omega type-T thermocouples are located between the different layers of the insulation. Heat losses from the sidewalls are neglected due to the absence of heat application to these sides. Each test plate contains two Omega type-T thermocouples enclosed in a metal sheath, which are installed so that wiring emerges on the sides of the test plates away from the air stream. Each thermocouple is installed so that it is located approximately 0.6 mm beneath the side of the test surface which is adjacent to the air stream. As shown in Fig. 3, thermocouples are positioned on the spanwise centerline of the test surface, either 123.5 mm or 246.9 mm from the leading edges of the test plates. All thermocouples employed in the study are calibrated using a Brinkmann Instruments LAUDA K-4/RD electronic water bath and an Omega model 5830 Thermister Thermometer as a temperature reference. The voltage produced by each thermocouple is measured using a HP44422T thermocouple card inserted into the same Hewlett-Packard data acquisition controller and extender used to acquire the voltage signals from the pressure transducers.

Energy balances are performed to determine magnitudes of convective heat flux for each test plate. Prior to this, as the test surface is warming up, the power to each heater is adjusted using a Powerstat type 1368 variac so that convective heat flux levels from both heaters are the same. The current moving through each circuit is measured using a Westinghouse type PU-5 F01350 ammeter. A Hewlett-Packard 3466A digital multimeter is employed to read the voltage drop across each heater. Temperature and power data are acquired when the test section is at thermal equilibrium, determined when temperatures along the surface change by less than about 1 °C over a five-minute period. Using the known power into each heater, the conduction loss through the insulation, and appropriate surface areas, and the convection heat flux q from each test surface is determined. The actual wall temperature t_w is determined from thermocouple measured temperatures, and estimates of temperature drop through the 0.6 mm of steel located between each thermocouple and the test surface. The local mixed mean temperature t_m is determined at each embedded wall thermocouple location using energy balances applied to the air stream between the entrance of the test section and each thermocouple location. The mixed mean temperature of the air stream at the inlet of the test section is measured using three thermocouples centered in the channel at a location which is approximately 50.8 mm upstream of the test section entrance. The local heat transfer coefficient h at each thermocouple location is then given by

$$h = q/(t_w - t_m). \tag{8}$$

Local Nusselt numbers are then determined using

$$Nu = hD_h/k, \tag{9}$$

where the air stream thermal conductivity k is based on test section inlet temperature. Local Stanton numbers at each surface thermocouple location are then given by

$$St = Nu/Re_{D_h} Pr \tag{10}$$

or, alternatively,

$$St = h/\rho C_p V, \tag{11}$$

where air density ρ is also based on static conditions at the inlet of the test section.

3.4. Experimental uncertainties

Uncertainty estimates are based on 95% confidence levels, and determined using procedures described by Moffat [7]. Uncertainty of temperatures measured with thermocouples is ±0.15 °C. Local Nusselt number, and local skin friction coefficient uncertainties are then about ±4.0%, and ±8.0%, respectively. Reynolds number uncertainty is about ±1.7% for Re_{D_h} of 20,000.

4. Experimental results

4.1. Skin friction coefficients, and equivalent sandgrain roughness magnitudes

Fig. 4 shows skin friction coefficients as dependent upon Reynolds number (based on hydraulic diameter) for the top and bottom plates of the channel, which are comprised of:

(i) *smooth* test surfaces,
(ii) *rough1* test surfaces,
(iii) *rough2* test surfaces.

This figure shows $C_f/2$ values which decrease with Re_{D_h} for each of these three test surfaces. At each Re_{D_h}, the *smooth* test plate gives the lowest $C_f/2$ values, and the *rough2* surface then gives the highest $C_f/2$ values. Notice that the smooth surface skin friction coefficients are in excellent agreement with values determined using a smooth duct correlation from Kays and Crawford [1].

To compare the rough surface data with existing correlations, coefficients of friction values must be determined which are representative of the rough test walls

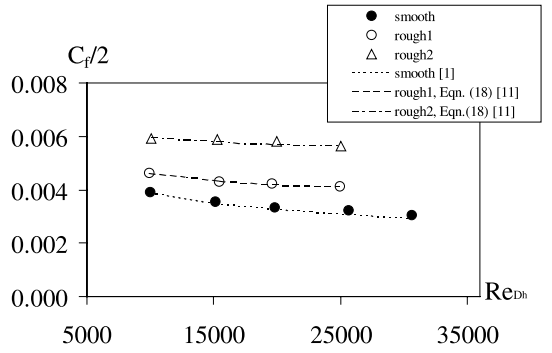

Fig. 4. Measured skin friction coefficients for the *smooth*, *rough1*, and *rough2* test surfaces along with values obtained from correlations [1,11].

only. To do this, the smooth wall surface shear at the same Reynolds number must first be determined. If $\Delta P/\Delta x$ is the average pressure drop per unit length, then the surface shear for all four smooth channel surfaces, τ_s is given by

$$\tau_s = (\Delta P/\Delta x)[bw/2(b+w)]. \tag{12}$$

With rough top and bottom walls and smooth sidewalls, the coefficient of friction (for the rough walls only) is then determined using τ_s, and the equations given by

$$bw\Delta P = 2b\Delta x\tau_s + 2w\Delta x\tau_r, \tag{13}$$

$$\tau_r = \left(\frac{b}{2}\right)\left(\frac{\Delta P}{\Delta x}\right) - \left(\frac{b}{w}\right)\tau_s, \tag{14}$$

and

$$C_f/2 = \tau_r/\rho V^2. \tag{15}$$

With this approach, the $C_f/2$ values given by Eq. (15) are unaffected by the sidewalls and are representative of the rough top and bottom test surfaces only. However, note that these corrected $C_f/2$ values are then also the same as for a duct with the same roughness on all four sides.

Magnitudes of equivalent sandgrain roughness k_s for the *rough1* and *rough2* test surfaces are determined using procedures described by van Rij et al. [8]. With this method, equivalent sandgrain roughness values are determined from roughness geometry (measured using a Wyko high-resolution optical Surface Profilometer, which determines surface contours using light interferometry), along with a modified version of the Sigal and Danberg [9,10] correlation, which is given by the following equations:

$$\frac{k_s}{k} = \begin{cases} 1.583\times10^{-5}\Lambda_s^{5.684}, & \Lambda_s \leqslant 7.842, \\ 1.802\Lambda_s^{0.0304}, & 7.842 \leqslant \Lambda_s \leqslant 28.12, \\ 255.53\Lambda_s^{-1.454}, & 28.12 \leqslant \Lambda_s. \end{cases} \tag{16}$$

These modified Eqs. (16) are determined from measurements made by van Rij et al. [8] for three-dimensional, irregular roughness, whereas the original equations, given by Sigal and Danberg, are for two-dimensional roughness [9,10]. Eq. (16) provides a good match to the experimental data for several types of roughness elements, including spheres, spherical segments, cones, and non-uniform, three-dimensional, irregular sandgrain-type roughness [8]. To determine Λ_s for three-dimensional roughness, the ratio of frontal area to windward wetted surface area of one roughness element (as originally recommended by Sigal and Danberg [9,10] for two-dimensional roughness) is replaced with the ratio of the total frontal area to the total windward wetted surface area for all the roughness elements on the surface, S_f/S_s. The roughness parameter Λ_s is thus modified to become

$$\Lambda_s = \left(\frac{S}{S_f}\right)\left(\frac{S_f}{S_s}\right)^{-1.6}. \tag{17}$$

To calculate the total frontal area, S_f, and the total wetted surface area, S_s, numerical data are employed, which are obtained using the optical surface profilometer, mentioned earlier. With these data, the rough surface is first numerically divided into finite element triangles. To calculate the total windward wetted surface area, S_s, the area of each surface triangle facing the direction of flow is summed. To calculate the total frontal area, S_f, each surface triangle facing the direction of flow is projected onto a plane perpendicular to the flow. The areas of all of these projected triangles are then summed. The final values of S_f and S_s are then used in Eq. (17) to determine the roughness parameter Λ_s. Eq. (16) is then employed to determine k_s/k.

To calculate the equivalent sand grain roughness size k_s, the roughness height k must then be known. For a rough surface with irregularly sized and spaced elements, each roughness element height is different and there is no defined zero, or base value, from which to measure this height. Therefore, the surface's average roughness element height is used for k. To calculate this average roughness element height, all of the roughness elements on the surface are aligned by their maximum point and the profiles are ensemble-averaged to get an average roughness element profile. From this profile, the average roughness element height is determined [8].

The procedures and accuracy of the numerical code used to calculate equivalent sandgrain roughness magnitudes, k_s values are verified by favorable comparisons of numerically determined values with values determined analytically for different rough surfaces, which consist of arrays of either cones or spherical segments [8]. Magnitudes of k_s for the *rough1* and *rough2* test surfaces are then 50.2 μm and 168.2 μm, respectively. For Re_{D_h} from 10000 to 25000, these then give roughness

Reynolds number values from 3.1 to 7.3 for the *rough1* surface, and from 11.5 to 27.9 for the *rough2* surface [8]. The magnitudes of k for the *rough1* and *rough2* surfaces are 85.14 μm and 85.14 μm, respectively. Magnitudes of parameter Λ_s for the *rough1* and *rough2* surfaces are 6.05 and 15.12, respectively [8].

With these values in hand, the experimental skin friction coefficients for the two rough test surfaces in Fig. 4 can be compared with values from the Colebrook [11] correlation for transitionally rough flow ($5 \leqslant Re_{k_s} \leqslant 70$). This equation is given by

$$\frac{C_f}{2} = \left[-2.46 \ln \left(\left(\frac{k_s/D_h}{3.7} \right) + \frac{0.887}{Re_{D_h}\sqrt{C_f/2}} \right) \right]^{-2}. \quad (18)$$

Fig. 4 shows that skin friction coefficient values, determined using k_s values from roughness geometry and Eq. (18), are in excellent agreement with measured skin friction coefficients (after the influences of the smooth sidewalls are removed).

4.2. Heat transfer results

Because heating is only applied to the top and bottom surfaces of the channel, the experimental Nusselt numbers and Stanton numbers are largely unaffected by the sidewalls of the channel, and are representative of the top and bottom test surfaces only. The Nusselt numbers presented here are determined from averages of the local values measured at the two thermocouple locations which are on opposite sides of the channel at each x location, 123.5 mm and 246.9 mm. Note that the two local Nusselt number values at each of these x locations are in close agreement for all experimental conditions investigated.

Nusselt numbers, averaged in this way, and measured on the *smooth* test plates, are shown in Fig. 5. Values increase continuously as the Reynolds number based on hydraulic diameter increases, with values at $x = 123.5$ mm slightly higher than values at $x = 246.9$ mm due to differences in thermal boundary layer development. Nusselt numbers determined from correlations given by Kays and Crawford [1] and Incropera and DeWitt [12] for ducts with smooth walls are included in Fig. 5, and are in reasonable agreement with each other, but are higher than measured values from the present study. This is because both correlations are for thermally fully developed duct flows with a constant heat flux boundary condition and heating around the entire duct circumference. In contrast, only the top and bottom walls of the present channel are heated (with the present sidewalls unheated).

Fig. 6 presents Nusselt numbers for all three types of test surfaces. Here, Nusselt numbers increase continuously with Re_{D_h} for each test surface, with higher rates of increase for the *rough1* and *rough2* surfaces, compared to the *smooth* surfaces. At each Re_{D_h}, the *smooth* test plates give the lowest *Nu* values, and the *rough2* test plates produce the highest *Nu* values. For each surface tested, the Nusselt numbers at $x = 123.5$ mm are slightly higher than values at $x = 246.9$ mm.

Stanton numbers for the same locations and test conditions are given in Fig. 7. In this case, average Stanton number values for $x = 246.9$ mm are presented because they are more representative of thermally fully developed flow than values measured at the upstream thermocouple location. Here, as before, the *smooth* and *rough2* test plates give the lowest and the highest Stanton numbers at each Reynolds number, respectively. Measured *St* are compared with values determined using the Dipprey and Sabersky correlation [3], which is given by Eq. (2), as well as the Kays and Crawford correlation [1], which is given by Eqs. (3) and (4). Values of *Pr* equal to 0.71, Pr_t equal to 0.90 and C equal to 1.00 are employed in these equations. Important differences are apparent in Fig. 7, since correlated Stanton numbers are generally higher than the measured *St* magnitudes. The only exception is apparent for the *rough1* experimental results, which are in approximate agreement with Eqs. (3) and (4) for $Re_{D_h} > 20\,000$.

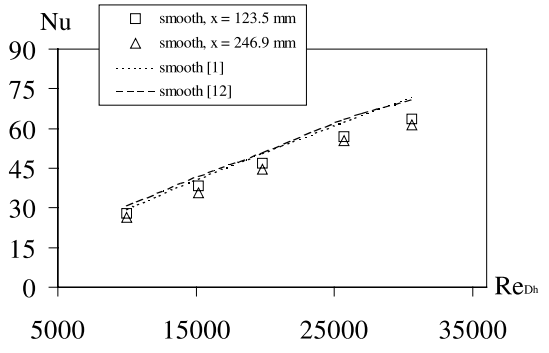

Fig. 5. Measured Nusselt numbers for the *smooth* test surfaces, along with values obtained from correlations [1,12].

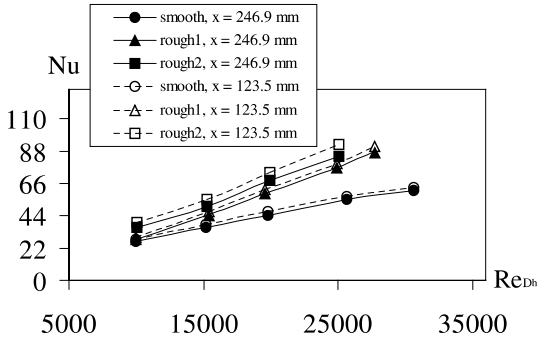

Fig. 6. Measured Nusselt numbers for the *smooth*, *rough1*, and *rough2* test surfaces.

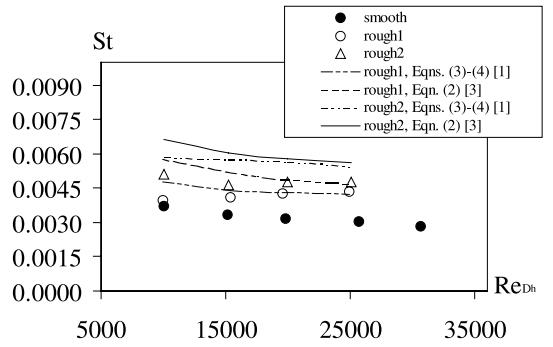

Fig. 7. Measured Nusselt numbers for the *rough1* and *rough2* test surfaces, along with correlation Eqs. (2)–(4) for rough surfaces [1,3]. *Smooth* surface experimental values are included for comparison.

4.3. Reynolds analogy results

Magnitudes of $St/(C_f/2)$ for all three sets of test surfaces (*smooth*, *rough1*, *rough2*) are now presented and discussed. Note that the St and $C_f/2$ values employed to deduce this ratio are each representative of the top and bottom surfaces of the channel only. Both quantities are thus based on the same test surface area. Here, average Stanton number values for $x = 246.9$ mm are again presented because they are more representative of thermally fully developed flow than values measured at the upstream thermocouple locations.

$St/(C_f/2)$ values for the smooth test surfaces are presented and compared to smooth surface Reynolds analogy equations from Kays and Crawford [1] and Incropera and DeWitt [12] in Fig. 8. This figure shows that each of these correlations is higher than the present data for all Reynolds numbers considered. In contrast, Eq. (1), which is considerably simpler than either of these correlations, provides a much better representation of the present *smooth* test surface data.

Fig. 9 shows the present *rough1* and *rough2* surface data compared to $St/(C_f/2)$ magnitudes deduced from Eq. (2) from Dipprey and Sabersky [3], and to $St/(C_f/2)$ magnitudes deduced from Eqs. (3) and (4) from Kays and Crawford [1]. Values of Pr equal to 0.71, Pr_t equal to 0.90, and C equal to 1.00 are employed in these equations for these comparisons. Important differences between these correlations and the present *rough2* surface data are apparent for all Re_{D_h}. In addition, at each Re_{D_h}, the *rough2* surface gives $St/(C_f/2)$ values which are *lower* than the smooth test plate values, and the *rough1* surface gives $St/(C_f/2)$ values which are generally *higher* than the smooth test plate values. This illustrates different increases in skin friction coefficients, relative to the increases in surface Stanton numbers, which are produced by the two different rough test surfaces. Fig. 10

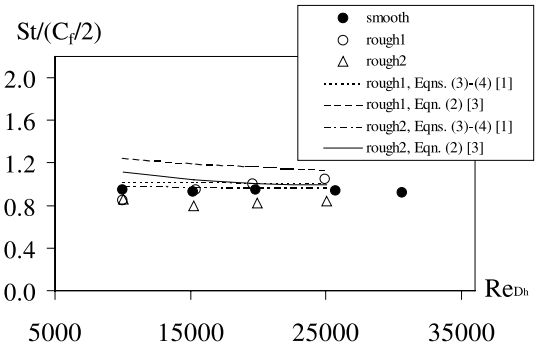

Fig. 9. Measured magnitudes of $St/(C_f/2)$ for the *rough1* and *rough2* test surfaces as dependent upon Reynolds number based on hydraulic diameter, along with correlation Eqs. (2)–(4) for rough surfaces [1,3]. *Smooth* surface experimental values are included for comparison.

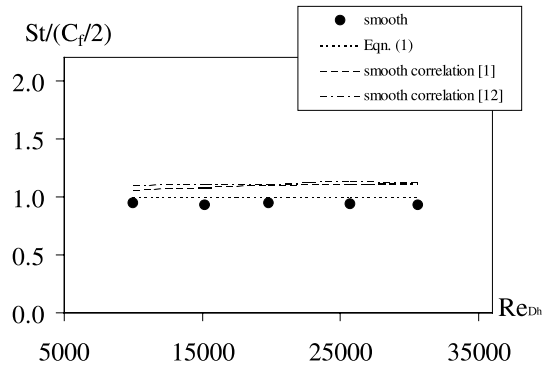

Fig. 8. Measured magnitudes of $St/(C_f/2)$ for the *smooth* test surfaces, along with Eq. (1), and values given by correlations for smooth surfaces [1,12].

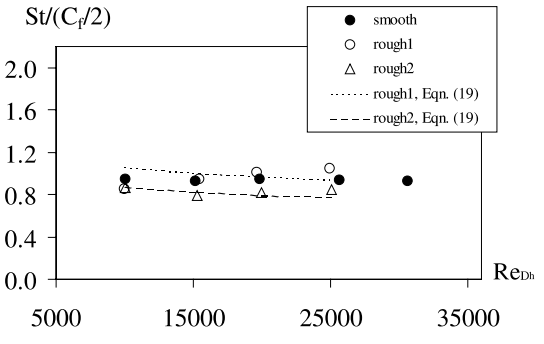

Fig. 10. Measured magnitudes of $St/(C_f/2)$ for the *rough1* and *rough2* test surfaces as dependent upon Reynolds number based on hydraulic diameter, along with Reynolds analogy equation (19) for real component surface roughness. *Smooth* surface experimental values are included for comparison.

shows that the present data from both rough test surfaces, as dependent upon Re_{D_h}, are more accurately represented by an equation having the form

$$St = \frac{C_f/2}{Pr_t + (C_f/2)^{0.1}(1/St_k - 1.00)}, \quad (19)$$

where Eq. (4) is employed to determine St_k with $C = 1.0$. Eq. (19) is thus a more accurate Reynolds analogy for surfaces with irregular, three-dimensional real component roughness, than that given by Eqs. (2)–(4). This is further illustrated by Fig. 11, which shows Eq. (19) compared to the present rough surface data, when plotted as dependent upon roughness Reynolds number, Re_{k_s}.

Note that Eqs. (2) and (3) are representative of granular close-packed roughness, some types of two-dimensional roughness, and uniform spheres roughness [1,3], whereas Eq. (19) is for three-dimensional, irregular roughness. The Reynolds analogies for these different types of roughness employ similar equations for the conduction sublayer Stanton number St_k. This indicates that the non-dimensional temperature drops (which exists across the semi-stagnate fluid around and between roughness elements, and within roughness cavities) have similar dependence upon the Prandtl number and roughness Reynolds number for these different types of roughness. The different coefficients in Eqs. (3) and (19) then indicate different effects of these non-dimensional temperature drops on turbulent transport of heat locally near the roughness elements. This is because of the different spreading of the conduction sublayer over surfaces with uniformly spaced and shaped roughness elements, compared to a surface with a spectrum of irregular roughness sizes and shapes. The latter situation also suggests different mixing mechanisms over a wider range of length scales, whereas a smaller distribution of mixing length scales are expected when one size of roughness elements is employed. Reynolds analogy equations thus have some dependence upon roughness geometry, as indicated by the different coefficients employed in Eqs. (3) and (19).

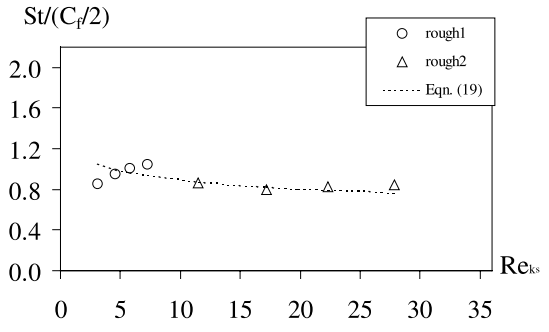

Fig. 11. Measured magnitudes of $St/(C_f/2)$ for the *rough1* and *rough2* test surfaces as dependent upon roughness Reynolds number, along with Reynolds analogy equation (19) for real component surface roughness.

4.4. Performance parameters

Magnitudes of the Gee and Webb [6] performance parameter, $(Nu/Nu_o)/(C_f/2/C_f/2_o)^{1/3}$, are presented in Fig. 12. According to these authors, this form of performance parameter is based on "equal pumping power and heat duty". Parameter magnitudes are generally about the same for the *rough1* and *rough2* test surfaces at each Reynolds number, except for a *rough2* value which is higher than the *rough1* value at Re_{D_h} of 10,000. Also included in Fig. 12 are lines which represent the smooth surface Reynolds analogy equation (1). The present *rough2* data lie below Eq. (1). *Rough1* data are below Eq. (1) for lower values of Re_{D_h}, and in approximate agreement with Eq. (1) for Re_{D_h} of 20,000 and above. Notice that performance parameters for the present rough surfaces have about the same magnitudes (but at lower Reynolds numbers) compared to some of the rib turbulator data from Han and Park [13]. The present data are then generally higher than $(Nu/Nu_o)/(C_f/2/\ C_f/2_o)^{1/3}$ magnitudes from a channel with pin fins [14], when compared at the same Re_{D_h}.

Additional performance information for the *rough1* and *rough2* test surfaces is given in Fig. 13, where Nu/Nu_o is shown as it depends upon $(C_f/2)/(C_f/2_o)$. The present *rough1* and *rough2* data move progressively away from the lower left-hand corner of the graph as Re_{D_h} increases, with the *rough2* data farther away from the corner than the *rough1* data. The present data generally lie just below or near Reynolds analogy Eq. (1) for smooth surfaces. Fig. 13 then also shows that the present rough surface Nu/Nu_o data are significantly below data

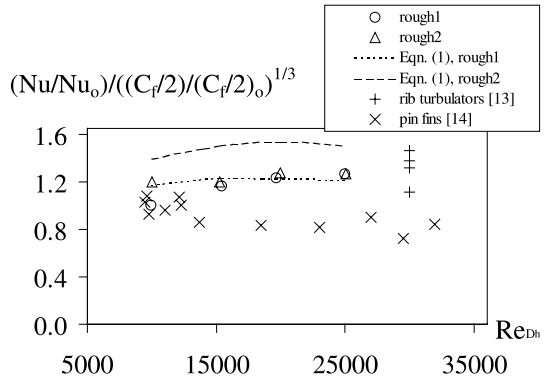

Fig. 12. Measured magnitudes of performance parameter $(Nu/Nu_o)/(C_f/2/C_f/2_o)^{1/3}$ for the *rough1* and *rough2* test surfaces as dependent upon Reynolds number based on hydraulic diameter, along with smooth surface Reynolds analogy equation (1). Data from [13,14] are included for comparison.

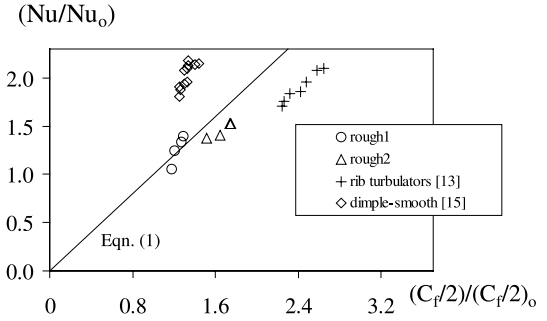

Fig. 13. Measured magnitudes of (Nu/Nu_o) as dependent upon $(C_f/2/C_f/2_o)$ for the *rough1* and *rough2* test surfaces, along with smooth surface Reynolds analogy equation (1). Data from [13] and [15] are included for comparison.

from a channel with dimples on one surface [15], when compared at the same $(C_f/2)/(C_f/2_o)$. Rib turbulator data from [13] give higher Nu/Nu_o, as well as higher $(C_f/2)/(C_f/2_o)$, compared to the present rough surface data.

5. Summary and conclusions

A new Reynolds analogy equation is developed for roughness which is similar to that which exists on the external surfaces of some turbine airfoils under extreme operating conditions, or on surfaces of other operating industrial devices, with deposit accumulation, such as heat exchangers. The equation, and the experimental results which are presented and employed to deduce this equation are then representative of the roughness which exists naturally as a result of common manufacturing, operation, and aging processes, rather than for the artificial roughness like that employed in many other experimental studies. Presented are local skin friction coefficients, local Nusselt numbers, and local Stanton numbers for a pair of polished smooth surfaces, and for two other pairs of surfaces with different levels of irregular, three-dimensional surface roughness. Performance parameters, and magnitudes of $St/(C_f/2)$ are also presented, after they are determined from measured quantities. All of these results are obtained for transitionally rough flows at Reynolds numbers (based on hydraulic diameter) from 10,000 to 25,000 in an internal channel with an aspect ratio of 8, arranged with the instrumented test plates installed on the two widest surfaces. Each of the measured parameters is thus based on the area of the top and bottom surfaces of the channel only.

Surfaces with real component surface roughness, with irregular, three-dimensional shapes and irregular distributions along the test surfaces, give a Reynolds analogy equation which is different from the ones associated with uniformly shaped roughness elements placed in a regular array with uniform spacing and arrangement. The new Reynolds analogy, for the three-dimensional, irregular roughness, is given by Eq. (19), and provides a good representation of $St/(C_f/2)$ values for this type of roughness. This new equation is also needed because Stanton numbers and Nusselt numbers, measured on surfaces with real component roughness, show important differences from existing correlations [1,3] for artificial man-made roughness, or uniformly shaped roughness elements arranged in a regular pattern. Eq. (19) is verified using air at atmospheric conditions. Additional experiments are needed to verify the accuracy of the equation for molecular Prandtl numbers which are significantly different from 1.0.

Acknowledgements

The research reported in this paper was sponsored by General Electric Corporate Research and Development Center, and by the National Science Foundation (NSF Grant Number CTS-0086011). Dr. Kent Cueman was the GE-CRD program monitor. Dr. Stefan Thynell and Dr. Richard Smith were the NSF program monitors. Dr. Ron Bunker is also acknowledged for several useful discussions which took place as the research was underway.

References

[1] W.M. Kays, M.E. Crawford, Convective Heat and Mass Transfer, third ed., McGraw-Hill, New York, 1993.
[2] N. Abuaf, R.S. Bunker, C.P. Lee, Effects of surface roughness on heat transfer and aerodynamic performance of turbine airfoils, ASME Trans. J. Turbomach. 120 (3) (1998) 522–529.
[3] D.F. Dipprey, R.H. Sabersky, Heat and momentum transfer in smooth and rough tubes at various Prandtl numbers, Int. J. Heat Mass Transfer 6 (1963) 329–353.
[4] G.I. Mahmood, M.L. Hill, D.L. Nelson, P.M. Ligrani, H.-K. Moon, B. Glezer, Local heat transfer and flow structure on and above a dimpled surface in a channel, ASME Trans. J. Turbomach. 123 (1) (2001) 115–123.
[5] C.R. Hedlund, P.M. Ligrani, Local swirl chamber heat transfer and flow structure at different Reynolds numbers, ASME Trans. J. Turbomach. 122 (2) (2000) 375–385.
[6] D.L. Gee, R.L. Webb, Forced convection heat transfer in helically rib-roughened tubes, Int. J. Heat Mass Transfer 23 (8) (1980) 1127–1136.
[7] R.J. Moffat, Describing the uncertainties in experimental results, Exp. Thermal Fluid Sci. 1 (1) (1988) 3–17.
[8] J.A. van Rij, B.J. Belnap, P.M. Ligrani, Analysis and experiments on three-dimensional, irregular surface roughness, ASME Trans. J. Fluids Eng. 124 (2002).
[9] A. Sigal, J.E. Danberg, New correlation of roughness density effect on the turbulent boundary layer, AIAA J. 28 (1990) 554–556.

[10] A. Sigal, J.E. Danberg, Analysis of turbulent boundary layer over rough surfaces with application to projectile aerodynamics, Army Ballistic Research Lab, Aberdeen Proving Grounds MD, Report No. BRL-TR-2977, 1988.
[11] C.F. Colebrook, Turbulent flow in pipes, with particular reference to the transition between the smooth and rough pipe laws, J. Inst. Civil Eng., London 11 (1938–1939) 133–156.
[12] F.P. Incropera, D.P. DeWitt, Introduction to Heat Transfer, third ed., Wiley, Canada, 1985.
[13] J.-C. Han, J.S. Park, Developing heat transfer in rectangular channels with rib turbulators, Int. J. Heat Mass Transfer 31 (1) (1988) 183–195.
[14] M.K. Chyu, Y.C. Hsing, T.I.-P. Shih, V. Natarajan, Heat transfer contributions of pins and endwall in pin-fin arrays: effects of thermal boundary condition modeling, ASME Trans. J. Turbomach. 121 (2) (1999) 257–263.
[15] G.I. Mahmood, P.M. Ligrani, Heat transfer in a dimpled channel: combined influences of aspect ratio, temperature ratio, Reynolds number, and flow structure, Int. J. Heat Mass Transfer 45 (10) (2002) 2011–2020.